

The Georgia Tech millimeter-wavelength measurement system and some applications to the study of planetary atmospheres

Kiruthika Devaraj¹ and Paul G. Steffes¹

Received 17 May 2010; revised 3 January 2011; accepted 20 January 2011; published 9 April 2011.

[1] With the advent of new millimeter-wavelength arrays such as the Atacama Large Millimeter Array capable of providing very precise maps of planetary emission, it becomes very critical to have an accurate knowledge of the millimeter-wavelength properties of gases under those planetary conditions. A millimeter-wavelength planetary atmospheric simulator and measurement system have been developed at the Georgia Tech Planetary Atmospheres Laboratory to accurately measure the propagation properties of gases under simulated planetary atmospheric conditions. The measurement system operates in the 2–4 millimeter-wavelength range and withstands up to 3 bars of pressure. It currently operates in the 190–300 K temperature range, and with minor modifications can operate in the 300–550 K temperature range for measurements of certain highly millimeter-wavelength-opaque gases. The measurements from this system can be used for developing accurate models of the millimeter-wavelength properties of gases under various planetary conditions which can then be used for retrieving the abundances of those gases through various remote sensing techniques.

Citation: Devaraj, K., and P. G. Steffes (2011), The Georgia Tech millimeter-wavelength measurement system and some applications to the study of planetary atmospheres, *Radio Sci.*, 46, RS2014, doi:10.1029/2010RS004433.

1. Introduction

[2] Millimeter-wavelength astronomy is an effective tool for studying the upper and the middle tropospheres of planetary atmospheres. Detailed investigation of the millimeter-wavelength absorptive and refractive spectra of various molecules can be used in the retrieval of accurate temperature structure and vertical profiles of abundances of these molecules, and sometimes even enable direct wind measurements from the determination of Doppler shift of the line centers [see, e.g., *Lellouch*, 2008]. The millimeter-wavelength range is often more sensitive than any other spectral range for the detection of minor species. To date, ground-based millimeter-wavelength observations have been extensively used for disk-averaged emission measurements of the jovian (outer) planets [*Griffin et al.*, 1986; *Muhleman and Berge*, 1991; *Griffin and Orton*, 1993; *Kramer et al.*, 2008], interferometric mapping of Saturn [*van der Tak et al.*, 1999; *Dunn et al.*, 2005], and interferometric mapping of Venus [*de Pater et al.*, 1991; *Sagawa*, 2008]. Future millimeter-wavelength observations with the Atacama Large Millimeter Array (ALMA) will represent a major step forward in the study of planetary atmospheres because of its high angular resolution, fast imaging capabilities, and wide instantaneous bandwidth. Combined millimeter-wavelength observations using the ALMA in conjunction with space

telescopes such as the Planck [*Lamarre et al.*, 2003] will greatly enhance studies of planetary atmospheres.

[3] Absorptivity data for planetary atmospheres obtained from ground-based and spacecraft-based observations can be used to infer abundances of millimeter-wavelength absorbing constituents in these atmospheres, as long as reliable information regarding the absorbing properties of potential constituents is available. Theoretical calculations of the absorption spectrum of gaseous molecules can be made from classical theories using resonant line strengths and frequencies which exist in spectral line catalogs such as the JPL catalog [*Pickett et al.*, 1998] or the GEISA catalog. However, these theoretical calculations of opacity are limited by the knowledge of the lineshapes and the broadening parameters of various molecules with the appropriate broadening agents under the temperature and pressure conditions found in planetary atmospheres. Hence, there is a need to make laboratory measurements of the properties of gases under simulated planetary atmospheric conditions over a range of temperatures and pressures that correspond to the altitudes probed by astronomical observations, and over a range of frequencies that correspond to those used in astronomical observations. These laboratory measurements can be used in the empirical determination of the self and foreign gas broadening parameters, temperature coefficients, and lineshapes of various gases under simulated planetary conditions. These laboratory measurements can also form the basis for developing accurate mathematical formalisms to model the millimeter-wavelength properties of gases under those planetary conditions.

[4] To facilitate such measurements, a millimeter-wavelength planetary atmospheric simulator and measurement

¹School of Electrical and Computer Engineering, Georgia Institute of Technology, Atlanta, Georgia, USA.

system have been developed at Georgia Tech. This system operates in the 2–4 millimeter-wavelength range and can be used to study the properties of various gases such as ammonia under Jupiter atmospheric conditions, sulfuric acid vapor under Venus atmospheric conditions, and hydrogen sulfide under Neptune atmospheric conditions. Although measurements have been made previously of the millimeter-wavelength properties of gases under planetary conditions [Joiner and Steffes, 1991; Fahd and Steffes, 1992; Fahd, 1992; Mohammed and Steffes, 2004], they were conducted at a limited number of frequencies and had large uncertainties. The high sensitivity of the measurement system described in this paper combined with its wide frequency range makes it a powerful tool for studying the millimeter-wavelength properties of gases under simulated planetary conditions.

2. Measurement Theory

[5] The reduction in the quality factor (Q) of a resonant mode of a resonator in the presence of a low-loss gas is used to measure the absorption of the gas [see, e.g., Hanley and Steffes, 2007]. The quality factor of a resonance is given by [Matthaei et al., 1980]

$$Q = \frac{2\pi f_0 \times \text{Energy Stored}}{\text{Average Power Loss}}, \quad (1)$$

where f_0 is the resonant frequency. The Q can be measured directly as the resonant frequency divided by its half-power bandwidth.

$$Q = \frac{f_0}{\text{HPBW}}. \quad (2)$$

[6] The Q of the lossy gas and its opacity are related by

$$\alpha \approx \frac{\varepsilon''\pi}{\varepsilon'\lambda} = \frac{1}{Q_{\text{gas}}} \frac{\pi}{\lambda}, \quad (3)$$

where ε' and ε'' are the real and imaginary permittivity of the gas, λ is the wavelength in km, and α is the absorptivity of the gas in Nepers/km. The quality factor of a resonator filled with the lossy gas is given by

$$\frac{1}{Q_{\text{loaded}}^m} = \frac{1}{Q_{\text{gas}}} + \frac{1}{Q_r} + \frac{1}{Q_{\text{ext1}}} + \frac{1}{Q_{\text{ext2}}}, \quad (4)$$

where Q_{loaded}^m is the measured quality factor of the loaded resonator, Q_{gas} is the quality factor of the gas under test, Q_r is the quality factor of the evacuated resonator, less coupling losses, and Q_{ext1} and Q_{ext2} are the external coupling losses in the resonator. For a symmetric resonator such as the one described in this paper, we can assume $Q_{\text{ext1}} = Q_{\text{ext2}}$. The coupling losses can be calculated by measuring the transmissivity $t = 10^{-S/10}$, where S is the insertion loss of the resonator in decibels (dB) at the frequency of a particular resonance, and using the relation [Matthaei et al., 1980]

$$t = \left[\frac{2Q_{\text{ext}}^m}{Q_{\text{ext}}} \right]^2, \quad (5)$$

$$Q_{\text{ext}} = \frac{2Q_{\text{ext}}^m}{\sqrt{t}}. \quad (6)$$

The value of Q_r is related to the measured Q at vacuum Q_{vac}^m by

$$\frac{1}{Q_{\text{vac}}^m} = \frac{1}{Q_r} + \frac{1}{Q_{\text{ext1}}} + \frac{1}{Q_{\text{ext2}}}. \quad (7)$$

Substituting equation (7) in equation (4), we get

$$\frac{1}{Q_{\text{gas}}} = \frac{1 - \sqrt{t_{\text{loaded}}}}{Q_{\text{loaded}}^m} - \frac{1 - \sqrt{t_{\text{vac}}}}{Q_{\text{vac}}^m}, \quad (8)$$

where t_{loaded} and t_{vac} are the transmissivities of the resonances in the loaded and vacuum conditions, respectively. The addition of the test gas causes a shift in the center frequency of the resonances corresponding to the refractive index of the test gas. There is a change in the quality factor of the resonances when the center frequency changes owing to the changes in coupling to the resonator. This effect is called dielectric loading [DeBoer and Steffes, 1994]. This effect can be removed by performing additional measurement of the quality factor of the resonances with a lossless gas and shifting the center frequency of resonances by the exact amount as the lossy gas. These matched measurements are used in place of the vacuum measurements in equation (8) and converting Nepers/km to dB/km (1 Neper/km = 8.686 dB/km), the absorptivity is given in dB/km as

$$\alpha = \frac{8.686\pi}{\lambda} \left(\frac{1 - \sqrt{t_{\text{loaded}}}}{Q_{\text{loaded}}^m} - \frac{1 - \sqrt{t_{\text{matched}}}}{Q_{\text{matched}}^m} \right). \quad (9)$$

The refractivity (N) of the test gas can be measured more directly than the opacity and is obtained from the refractive index of the gas (n) using

$$N = 10^6(n - 1). \quad (10)$$

Refractivity is measured by the change of the center frequency of the resonances compared to their vacuum values and is calculated using

$$N_{\text{measured}} = 10^6 \left(\frac{f_{\text{vac}} - f_{\text{gas}}}{f_{\text{gas}}} \right), \quad (11)$$

where f_{vac} and f_{gas} are the center frequency of the resonances when the system is under vacuum and filled with the test gas, respectively. This measured refractivity represents the total refractivity of the test mixture which is the sum of the individual constituents' refractivities weighted by their mole fraction. Refractivity depends on pressure (P) and temperature (T), and the normalized refractivity (independent of such dependences) is calculated as

$$N' = \frac{NRT}{P}, \quad (12)$$

where R is the universal gas constant.

3. Measurement System

[7] The measurement system consists of a planetary atmospheric simulator, millimeter-wavelength subsystems (W band/F band), and a data handling subsystem. The W band system

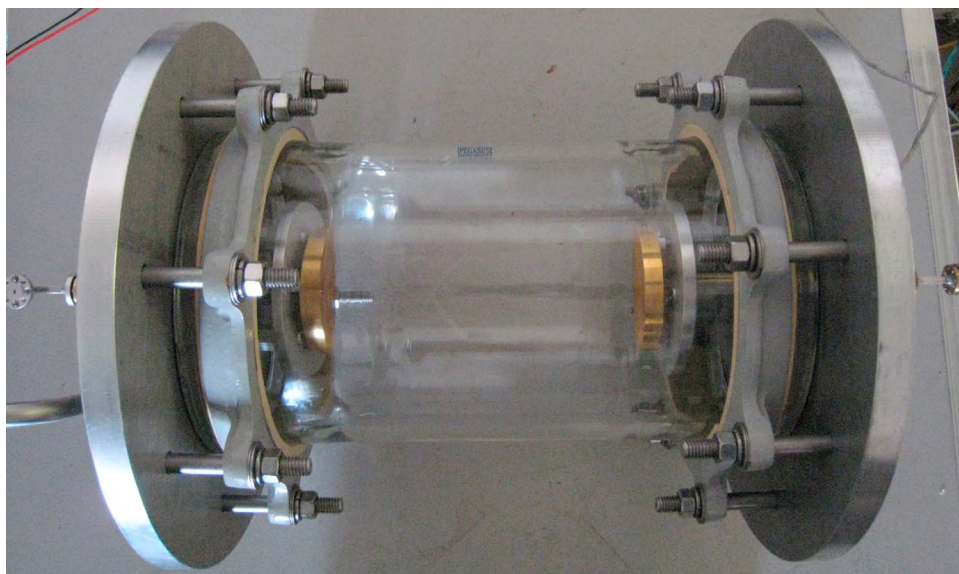


Figure 1. A picture of the glass pressure vessel enclosing the Fabry-Perot resonator used for simulating the jovian atmospheric conditions.

is used for measurements in the 3–4 millimeter-wavelength range and the F band system is used for measurements in the 2–3 millimeter-wavelength range.

3.1. Planetary Atmospheric Simulator

[8] The planetary atmospheric simulator controls and monitors the environment experienced by the measurement system, including the pressure and temperature conditions of the gas under test. The simulator consists of a pressure vessel, temperature chamber, gas-handling subsystem, and various measurement gauges. The main component of the atmospheric simulator is a pressure vessel capable of withstanding pressures up to 3 bars. This pressure vessel is a Pegasus® conical glass pipe (6x9 inches) with aluminum endplates. The endplates are sealed with Viton® O-rings sandwiched between the lip of the glass and the flat endplate which is bolted to an inner flange. The pressure vessel encloses the Fabry-Perot resonator used for making measurements and is shown in Figure 1. The temperature chamber has a stability of approximately $\pm 0.5^\circ\text{C}$.

[9] The pressure vessel and a part of the millimeter-wavelength measurement system are contained in a temperature-controlled chamber which is a Revco® ultralow-temperature freezer capable of operating between 173 K and 218 K. The freezer does not operate warmer than 218 K and hence measurements cannot be performed in the 218–290 K range. Room temperature measurements are also performed with the system placed inside the temperature chamber (with the cooling system shut-off) since the chamber helps to maintain thermal stability. When the system is operating at cold temperatures, the thermal stability is increased by placing iron blocks inside the freezer so that the temperature fluctuations inside the pressure vessel do not exceed $\pm 0.5^\circ\text{C}$ as verified by in situ temperature measurements. The temperature inside the pressure vessel is monitored by an Omega® Model HH21 Microprocessor Thermometer (display unit) connected to a Type-T (copper/copper-nickel) thermocouple probe threaded into a 1/4" NPT fitting on one side of the aluminum endplate

of the resonator. This allows the probe to be in direct contact with the test gases and provides a very accurate measurement of the temperature inside the vessel. The thermometer display unit has a resolution of 0.1°C and a 3σ accuracy of 0.3% of the displayed value plus an additional $\pm 0.6^\circ\text{C}$ uncertainty at temperatures below 0°C . Above 0°C , the additional uncertainty remains the same, but the accuracy improves to 0.1%. The thermocouple itself has an accuracy of 1.0°C or 0.75% of the reading, whichever is greater.

[10] Pressure measurements in the 2–3 bar range are made with an Omega® DPG7000-30 Digital Test Gauge, and pressure measurements in the 0–2 bar range (vacuum to 2 bars) are made with an Omega® DPG7000-VAC/15 Digital Test Gauge. These gauges have a resolution of 1 mbar and 0.05% full-scale total error band accuracy. The gauges only display differential pressure between the closed system and the ambient laboratory environment, and hence the gauge readouts can vary as the ambient pressure varies even if the absolute pressure in the system remains constant. To correct for this effect, digital barometers (Davis® Weather Monitor II 7440 and Young® 61202L) are used to measure the ambient pressure inside the laboratory.

[11] A Welch DuoSeal® vacuum pump Model 1376B-01 is used to evacuate the gases from the system from 1 bar down to vacuum. Gases at higher pressures are vented through an exhaust valve. A glass cylinder with a volume of approximately 7.2 L is connected to the system along with an Analytical Technology, Inc. PortaSens II portable gas leak detector capable of detecting trace amounts of gases through a series of interchangeable electrochemical cartridge sensors. Gases are fed into the pressure vessel through a series of regulators and valves. All components in the gas handling system are connected with seamless 3/8" outer diameter stainless tubing and Swagelok® fittings.

3.2. Millimeter-Wavelength Subsystem

[12] Currently, the 2–4 millimeter-wavelength measurements are made with two different subsystems, namely the

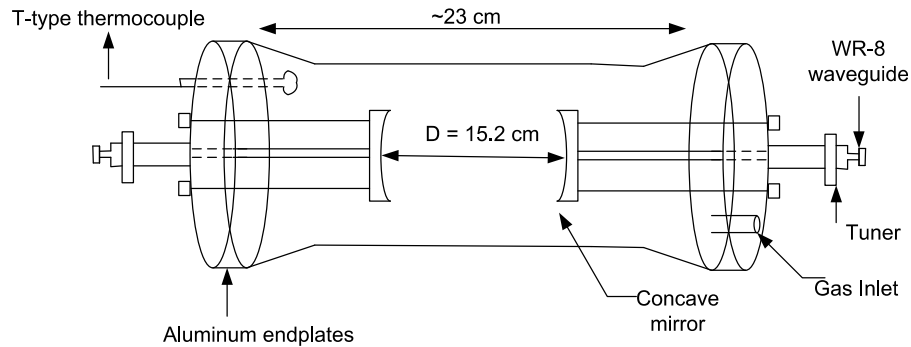


Figure 2. Block diagram of the near-confocal Fabry-Perot resonator.

W band and F band systems. At the heart of both the measurement systems is a spherical mirror Fabry-Perot resonator (FPR) in a near confocal configuration enclosed in the pressure vessel.

3.2.1. Fabry-Perot Resonator

[13] Resonant microwave cylindrical cavities have been used to observe molecular resonances in gases and their absorption coefficients for over 50 years [Bleaney and Penrose, 1947; Weidner, 1947; Gordy, 1948]. In the millimeter-wavelength region, FPRs provide low loss, high coupling efficiency, and high precision in measurements [Culshaw, 1960, 1961, 1962; Zimmerer, 1963]. FPRs have been successfully employed for the measurement of atmospheric gas losses in the millimeter-wavelength range for more than 40 years [see, e.g., Valkenburg and Derr, 1966]. Absorptivity of gases under simulated planetary conditions has also been measured using FPRs in the past [see, e.g., Joiner and Steffes, 1991; Fahd and Steffes, 1992].

[14] The FPR used in the millimeter-wavelength system described in this paper (Figure 2) consists of two concave gold-plated mirrors whose surface is polished to μm tolerance. Electromagnetic energy is coupled to and from the resonator (which acts as a band-pass filter) through irises located in the center of each of the mirrors via WR-8 waveguides which pass through the endplates to the exterior of the pressure vessel. The end of each waveguide section is pressure-sealed by a circular piece of mica window held in place by a low-temperature O-ring and vacuum grease. The resonator is symmetrical and the input/output ports are interchangeable. One of the ports is connected to the signal source through a waveguide section and the other end is connected to a high-resolution spectrum analyzer through a harmonic mixer and diplexer.

[15] The spherical mirror FPR is used in a near-confocal configuration. This configuration provides a number of advantages such as high quality factor and very good tolerance to the alignment of mirrors [Herriott *et al.*, 1964]. The radius of curvature (R) of the spherical mirrors is approximately 30 cm and the distance of separation (D) between the mirrors is adjustable thereby making it possible to measure resonances (transmission peaks) at desired frequencies. For the measurements that were made with this resonator, a mirror spacing of approximately 15.2 cm provided minimum diffraction losses and optimal free spectral

range (FSR). FSR is the frequency interval between adjacent axial mode resonances and is given by

$$\text{FSR} = \frac{c}{2D}, \quad (13)$$

where c is the speed of light. For the current resonator setup, $\text{FSR} \sim 1 \text{ GHz}$.

[16] There are three kinds of losses in an FPR: resistive losses (on the surfaces of the mirrors), coupling losses (due to the energy coupling in/out of the resonator through the irises), and diffraction losses (around the sides of the mirrors) [Culshaw, 1960, 1962]. When a spherical mirror interferometer is illuminated by an off-axis ray of light, the repeated reflections cause several raypaths and these raypaths give rise to additional resonances [Herriott *et al.*, 1964]. These additional off-axis resonances adversely affect the performance of the interferometer. Furthermore, diffraction loss is caused by energy spilling over the sides of the mirrors because of poor mirror alignment. To suppress the off-axis resonances and to reduce diffraction losses, the mirrors need to be very precisely aligned. This was achieved using a beam from a helium-neon laser, which was directed to the input waveguide of the resonator. The other mirror was adjusted so that the reflected beam focused precisely on the output iris. The coupling losses are a function of frequency because of the standing waves between the input/output irises and the signal source/detector. The coupling losses were reduced by ensuring a good waveguide to mirror joint. The resistive losses were minimized by using highly reflective gold-plated mirror surfaces with minimal surface irregularities. However, the mirror resistive losses increase at higher frequencies because of the shallow skin depth of the gold-plated mirrors. The coupling losses also increase at higher frequencies. Neglecting diffraction losses, the quality factor of the resonances are dependent on the mirror resistive and coupling losses. For the resonator described in this paper, the mirror resistive and coupling losses increase faster as a function of frequency compared to the theoretical increase in Q as a function of frequency, and become dominant at higher frequencies. Hence, the quality factor of the system decreases as a function of frequency (Figure 3).

[17] In order to achieve high system sensitivity (which corresponds to a high Q), all losses in an FPR should be minimized. After the alignments were made, the quality

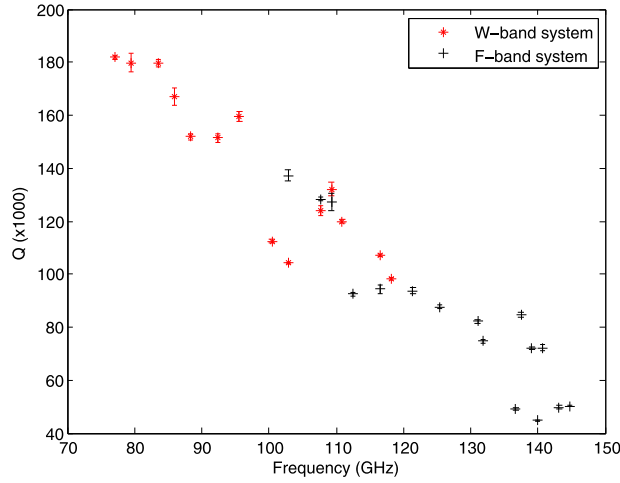


Figure 3. Quality factor of the resonances of the Fabry-Perot resonator measured at vacuum and room temperature ($T = 297$ K).

factor of the resonator at vacuum and $T = 297$ K in the 2–4 millimeter-wavelength range was between 45,000 and 190,000 (Figure 3). The effective path length (EPL) of the electromagnetic energy is given as [Valkenburg and Derr, 1966]

$$\text{EPL} = \frac{Q\lambda}{2\pi}. \quad (14)$$

[18] For example, consider a resonance at 77.08 GHz (3.89 mm). The observed Q of this particular resonance was 185,800. Hence, the effective path length is about 115.01 m. Figure 4 shows a plot of the effective path length of the resonances as a function of frequency measured at room temperature. The performance of the FPR improves slightly at lower temperatures.

3.2.2. W Band System

[19] The W band measurement system is used to measure the 3–4 millimeter-wavelength properties of gases, and is shown in Figure 5.

[20] A swept signal generator (HP 83650B) is used to generate signals in the 12.5–18.3 GHz range that are fed to a times six active multiplier chain (AMC) via flexible, low-loss, high-frequency 2.9 mm male–2.9 mm male coaxial cable assembly. All coax connections are tightened with an 8 in-lb (0.90 N-m) torque wrench to ensure reliable connections. The operating temperature of the AMC is 0°C – 45°C . Hence, the AMC is heat sunk to keep the case temperature below $+45^{\circ}\text{C}$ when it is used at room temperature. When the AMC is used at cold temperatures, the heat sink is removed and thermal insulation is provided so that the heat generated by the AMC could sustain its own operation even if the external temperature is -100°C . The AMC is hermetically sealed to prevent ice deposition at cold temperatures. The output from the AMC is fed to one of the ports of the FPR via a solid WR-8 waveguide section.

[21] The radio frequency (RF) signal from the output port of the FPR is fed to a QuinStar Technology QMH series harmonic mixer via solid WR-8/WR-10 waveguide sections so as to enable down-conversion of 3–4 millimeter-wavelength signal. The QMH series harmonic mixer has a

common SMA port for LO and IF signals, and hence an external diplexer (model MD1A) is used to combine/separate local oscillator (LO) and intermediate frequency (IF) signals. The typical conversion loss of this mixer is approximately 40 dB. Both the mixer and the diplexer are hermetically sealed when used in the freezer. The harmonic mixer locked to the 18th harmonic is used in the “external mixer” mode with a spectrum analyzer (HP 8564E). The detector within the spectrum analyzer operates in a positive peak mode, which displays the maximum power level received during the integration time of each point on each individual sweep. This mode is used primarily because it maximizes the data return to the computer. The normal mode detects both the high and low signal (noise floor) intensities at each frequency point, but when transferring to the computer, the spectrum analyzer is limited to 601 points in both the frequency and amplitude axes. In the normal mode, the peak level data becomes interspersed with the noise floor data, which would result in only half the data transferred being of practical use for these measurements and consequently would halve the frequency resolution. The mixer can also be used as a down-converter with an external local oscillator, but a different diplexer is used (model MD2A).

[22] As shown in Figure 5, the AMC and the harmonic mixer are placed as close to the resonator input/output ports as possible to reduce the signal loss and increase the signal to noise ratio of the resonances. The signal power generated by the signal source, the loss through the FPR, and the conversion loss of the mixer are dependent on the frequency. Hence, the signal to noise ratio of the received signal is also dependent on the frequency. For example, the swept signal generator is used to generate a 10 dBm signal at 12.5 GHz. This is fed to the AMC, which produces the RF signal at 75 GHz with a signal power of 5 dBm. At 75 GHz, the loss through the FPR is approximately 20 dB and the conversion loss of the mixer is 40 dB. Hence, the signal power that reaches the spectrum analyzer is approximately -55 dBm at 75 GHz.

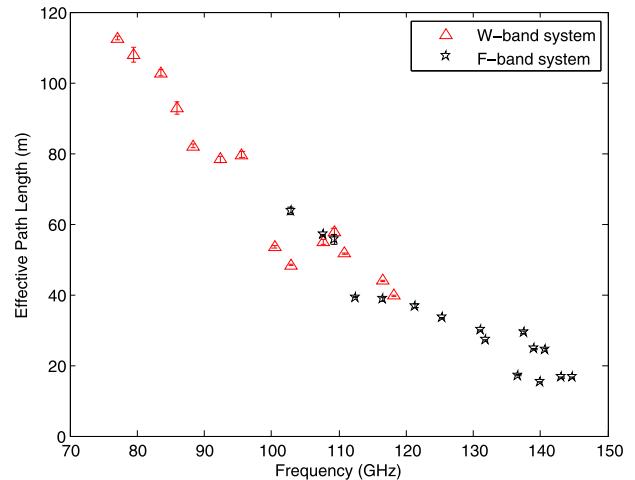


Figure 4. Effective path length of the resonances of the Fabry-Perot resonator measured at vacuum and room temperature ($T = 297$ K).

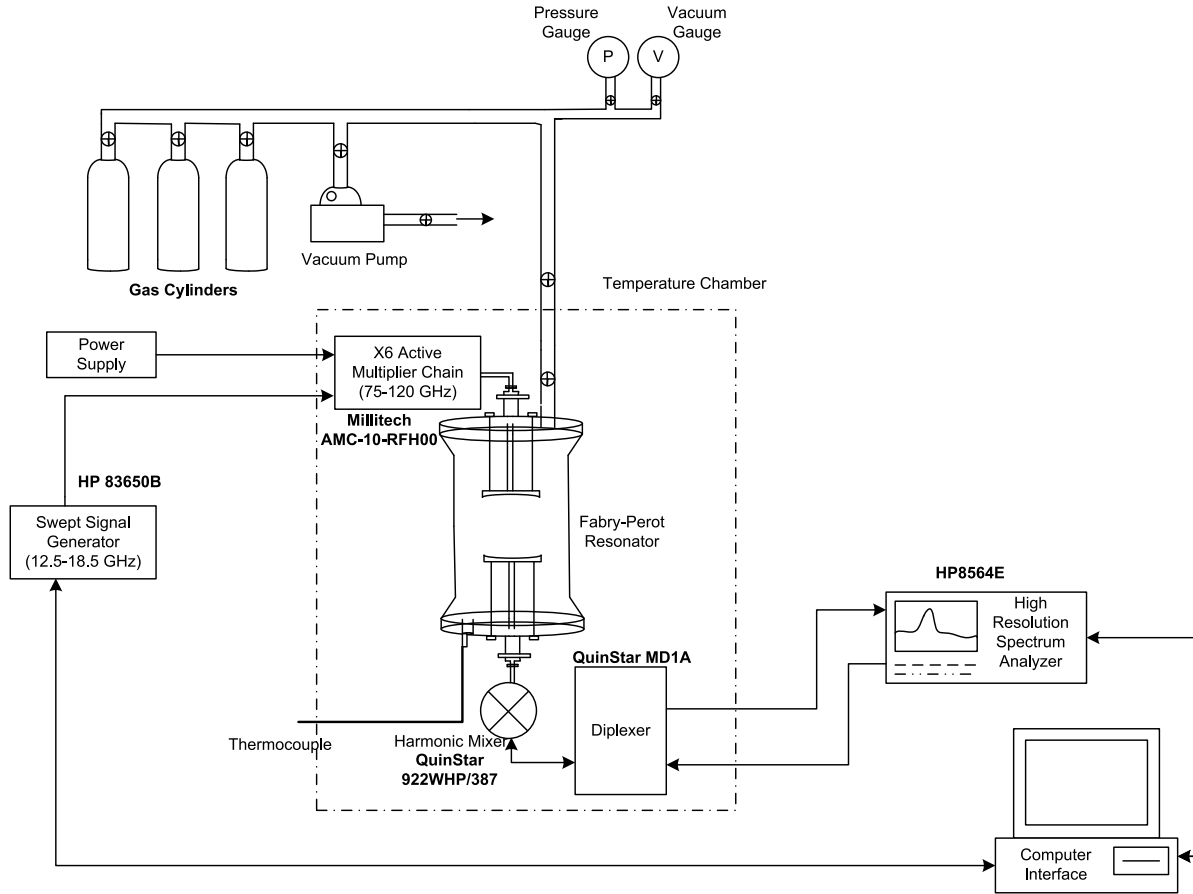


Figure 5. W band measurement system for studying gas properties under simulated planetary conditions. Solid lines represent the electrical connections, and the arrows show the direction of signal propagation. Valves controlling the flow of gases are shown by the small crossed circles.

3.2.3. F Band System

[23] The F band measurement system is used to measure the 2–3 millimeter-wavelength properties of gases and is shown in Figure 6.

[24] The signal generated by a swept signal generator (HP 83650B) in the 33–50 GHz range is amplified (Spacek model SG 4413-15-16W) and fed to a frequency tripler. To facilitate the operation of the amplifier inside the freezer, the heat sink mounted on the amplifier is removed and adequate thermal insulation is provided. Both the amplifier and the tripler are hermetically sealed while operating at cold temperatures. The output from the tripler is fed to one of the ports of the FPR via a solid WR-8 waveguide section.

[25] The RF signal from the output port of the FPR is fed to a harmonic mixer (Pacific Millimeter Products model DM) via a solid WR-8 waveguide section to enable down-conversion of 2–3 millimeter-wavelength signal. The harmonic mixer can operate with an LO frequency as high as 18 GHz and has a common SMA port for LO and IF signals, and hence an external diplexer (model MD2A) is used to combine/separate LO and IF signals. For a particular RF and IF frequency, LO frequency can be computed using

$$f_{LO} = \frac{f_{RF} - f_{IF}}{N}, \quad (15)$$

where N is the lowest integer such that $f_{LO} < 18$ GHz. The harmonic mixer has one diode, and requires a DC return path for the diode current. This DC return path follows the IF path in the diplexer, and the device attached to the IF port of the diplexer must have provision for a bias-tee. Mixer conversion loss is dependent upon the frequency, the harmonic number, applied LO power, and the diode current. For the 10th harmonic (LO frequency = 11–17 GHz for RF = 110–170 GHz) conversion loss is approximately 40 dB. Sensitivity of the receiver system will depend on the receiver bandwidth, but the mixer conversion loss sets a minimum noise contribution for the receiver system of 40 dB. If the internal spectrum analyzer local oscillator (3–6 GHz) is used, an even higher conversion loss associated with the low LO frequency and high harmonic mixing number results. Hence, a separate CW signal generator (HP 83712B) along with an amplifier (JCA Technologies model JCA 1920-612) are used as the LO, and harmonics less than the tenth order are used. The IF signal is then enhanced using a low noise amplifier (MITEQ model AMF-3F-012017) and displayed on the spectrum analyzer. The IF is chosen such that there is minimal radio frequency interference (RFI). RFI is further mitigated by wrapping aluminum foil tapes around the microwave components and connectors at the IF end.

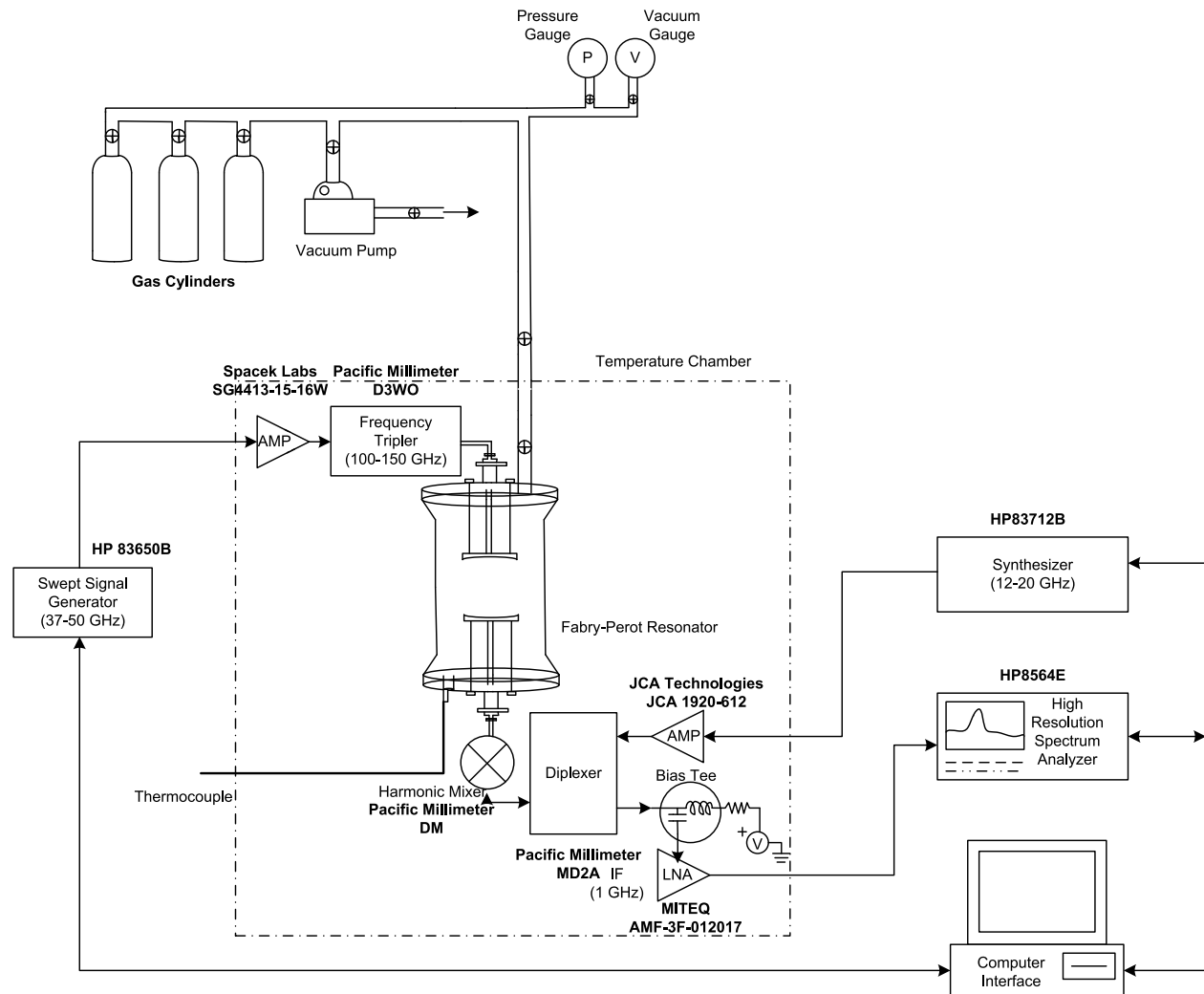


Figure 6. F band measurement system for studying gas properties under simulated planetary conditions. Solid lines represent the electrical connections, and the arrows show the direction of signal propagation. Valves controlling the flow of gases are shown by the small crossed circles.

3.3. Data Handling Subsystem

[26] The data acquisition system consists of a computer connected to the spectrum analyzer (HP 8564E), swept signal generator (HP 83650B), and CW signal generator (HP 83712B) via a general purpose interface bus (National Instruments GPIB Controller for Hi-Speed USB). The instruments are controlled via Matlab® and the Standard Commands for Programmable Instruments (SCPI). The software used is similar to that used by *Hanley and Steffes* [2007] with modifications to account for the suite of instruments used in this measurement system.

4. Measurement Procedure

[27] One of the most important prerequisites for performing the measurements of gas properties is a leak-proof system. Leak-proofing the system not only reduces the uncertainties in the experiments, but also ensures that no toxic or flammable gases leak from the system and pose a health hazard. The assembled pressure vessel, gas handling pipes, valves, and gas regulators are positive pressure-

tested with a liquid leak detection compound at three bars of pressure. Further tightening of the pressure vessel is achieved after drawing a vacuum since there is additional compression force on the surface of the pressure vessel due to normal atmospheric pressure. The pressure vessel has several junctions and joints where different types of materials meet (e.g., brass waveguide seals with an aluminum endplate via a low-temperature O-ring and vacuum grease). At low temperatures, there is differential contraction of the materials at the junctions depending on the materials' coefficient of thermal expansion and this increases the risk of leaks. To ensure a tight seal at low temperatures, the pressure vessel is evacuated and placed in the freezer until the desired temperature is reached and then quickly removed from the freezer and a third round of tightening is done. (It must also be ensured that the sudden exposure to ambient conditions while tightening does not crack the glass pressure vessel.) After the final tightening is completed, the pressure vessel is placed in the freezer and positive pressure-tested with an ultralow-temperature leak detection compound (Cantescor®) after the desired system temperature is reached. Once a good

seal is established, the pressure vessel is filled with three bars of argon and the pressure is monitored for several days to ensure that there is a good pressure seal. Once the pressure vessel is sealed at the coldest operating temperature, it remains leak-proof at warmer temperatures since warming expands the materials, and this only improves the seal.

[28] Once a good pressure seal is established, the measurement process begins by characterizing the resonances of the FPR at the measurement temperature. Whenever the temperature of the FPR changes, the metal standoffs that hold the mirrors in place and the mirrors themselves expand/contract, and hence the distance between the mirrors and their alignment change slightly. Any change in mirror alignment affects the off-axis resonances which move in frequency with respect to the axial mode resonances. As a result, some axial mode resonances become contaminated with the off-axis resonances, resulting in compound asymmetric resonances. Asymmetry (A) is defined as

$$A = 100 \frac{(f_{\text{high}} - f_{\text{center}}) - (f_{\text{center}} - f_{\text{low}})}{(f_{\text{high}} - f_{\text{low}})} \% \quad (16)$$

[DeBoer and Steffes, 1994], where f_{high} , f_{center} , f_{low} , represent the higher-frequency half power point, center frequency, and lower-frequency half power point of the resonances, respectively. Since asymmetric resonances might broaden disproportionately when lossy gases are added, only those resonances with $A \leq 5\%$ are used for making measurements. About a dozen high-Q, low-asymmetry resonances that are roughly uniformly spaced in frequency are selected to be used as the “standard resonances” for all the measurement cycles at a particular measurement temperature.

[29] Owing to the difficulties in frequently changing the measurement temperature, and because changes in pressure and mixing ratios can be achieved quickly, the gas properties in the 2–4 millimeter-wavelength range are measured at a particular temperature for different sets of mixing ratios and gas pressures. Once the desired set of measurements are performed at a particular temperature, the temperature of the chamber is changed and a new set of measurements are made at the new temperature.

[30] When gas molecules are added to the pressure vessel, they have a tendency to adhere (physically or chemically adsorb) to the surface of the pressure vessel. Physisorption is the process of gaseous molecules of one substance, the adsorbate, adhering to the surface of a liquid or solid substance, the substrate, due to weak attractive van der Waals forces between the adsorbate and the substrate. This does not result in any sharing of electrons and is not to be confused with chemisorption that requires the formation of a chemical bond between the substrate and the adsorbate. The formation of physically adsorbed layer may be likened to the condensation of a vapor to form a liquid and most likely occurs when the gas is near its condensation point, but can occur under warmer, lower pressure conditions [Young and Crowell, 1962]. If p is the equilibrium pressure of the adsorbed film and p_0 is the saturation vapor pressure of the gas at the experimental temperature, then below $p/p_0 = 0.01$ no significant adsorption takes place [Young and Crowell, 1962]. While all molecules can encounter physisorption, polar molecules are more prone to it, especially when the substrates are conductors. An analogue is a dipole interact-

ing electromagnetically with its image in the plane of the conductor. Adsorbed molecules have limited degrees of freedom and hence do not interact with the incident electromagnetic energy to the extent they would in the gaseous phase. Adsorbed molecules, however, do change the electrical conductivity of the surfaces, to which they adsorb [Young and Crowell, 1962]. In this measurement system, the effect of adsorbed ammonia was found to have a negligible effect on the conductivity and resulting Qs of the resonator. Desorption is the process by which the adsorbed molecules are returned to the gas phase. The most effective ways for molecules to desorb are by the reduction of the partial pressure of the adsorbate or by the increase of the temperature of the substrate to provide enough energy for the adsorbate to break the weak attractive van der Waals forces that hold them in place.

[31] A particular example of ammonia adsorption/desorption is discussed further and it should be noted that most polar molecules behave in a similar fashion. A study by *Rodrigues and Moraes* [2002] found that at all temperatures the physisorption capacity of ammonia increased with increasing ammonia concentration, but an increase in temperature at any concentration led to a decrease in the adsorption capacity of ammonia. The study also concluded that the effect of temperature more significantly affected desorption than that of ammonia concentration. Nonpolar molecules such as hydrogen and helium on the other hand do not adhere to the substrate at our experimental conditions. It is difficult to quantify or predict adsorption due to its dependence on the fine molecular structure of the substrate. Hence, precautions must be taken to account for adsorption, whenever gas mixtures are added to the system where one component adsorbs more than another. Earlier studies of ammonia opacity made under simulated jovian conditions did not properly account for adsorption [Mohammed and Steffes, 2004; Spilker, 1990]. When manufactured mixtures of hydrogen, helium and ammonia are used [e.g., Mohammed and Steffes, 2004], some ammonia in the mixture adsorbs to the surface of the measurement system thereby reducing its concentration in the gas phase, and there is no effective method to determine the exact concentration of ammonia left in the measurement system. When a series of progressive dilutions are employed to arrive at mixtures with a small ammonia concentration [Spilker, 1990], there is a shift in the adsorption/desorption equilibrium since the concentration of ammonia decreases after partial venting. This leads to additional desorption and disproportionate increase of the concentration of that gas.

[32] One way to compensate for adsorption is to presaturate the surface of the measurement system with the adsorbate so that no more adsorption occurs since there are only so many layers of adsorbate that can form on the substrate. This is achieved by adding ammonia to the pressure vessel first and letting the system completely saturate while simultaneously monitoring the Qs of the resonances. After ammonia is added, there is a reduction in the Qs of the resonances because of the absorption of electromagnetic energy by ammonia in the gas phase. Once ammonia starts adhering to the surface of the resonator, its concentration is reduced and hence the Qs increase. After ammonia completely saturates the surface of the pressure vessel, the Qs stabilize, and at this stage adsorption equals desorption. After this stage, hydrogen and helium are added to the system. Measurements of gas properties are made starting at the lowest pressure by adding

ammonia and working up to higher pressures by adding hydrogen and helium. Measurements are never made by venting the gas mixture down to lower pressures because of the possibility of enhanced ammonia desorption from the substrate due to the reduction in the partial pressure of ammonia that leads to a disproportionate increase in the concentration of ammonia.

[33] Each measurement cycle consists of first measuring the preselected standard resonances of the FPR at vacuum. Test gases (e.g., ammonia, hydrogen and helium) are added to the system and the frequency shifted resonances are measured at different pressures. The system is then vented down to the ambient pressure and a vacuum is drawn for several hours to remove the test gases. To ensure complete removal of ammonia from the system, argon is added to the pressure vessel and a sample is drawn in a glass cylinder equipped with an ammonia sensor. If the sensor detects ammonia, a vacuum is drawn for a few more hours. The process is iterated until ammonia is no longer detected by the sensor. A second set of vacuum measurements of the resonances is made. A nonabsorbing gas such as argon or carbon dioxide is added to the system to shift the frequency of the resonances by the exact same amount as the test gases and the dielectrically matched measurements are made. The system is evacuated once again to remove the matched gas and a third set of vacuum measurements are made. After this step, the W band/F band signal generator and detector are disconnected from the resonator and three sets of straight-through transmissivity measurements are made under the same conditions at each pressure/frequency point of the test gas. Each transmissivity measurement consists of coupling 1/100th of the RF signal power (via a WR-10 20-dB directional coupler) from the generator to the detector and making multiple measurements at the standard resonant frequencies. Between the transmissivity measurements, all the waveguide/coax connections are disconnected and reconnected to better statistically characterize the reproducibility of the electrical connections. Transmissivities are only measured at the end of the experiments so as to ensure that the resonator stays at a constant temperature ($\pm 0.5^\circ\text{C}$) throughout the measurement cycle. (Transmissivity measurements involve opening the temperature chamber multiple times to disconnect/reconnect the signal generator, detector, waveguides, and coax assembly, and this might temporarily alter the temperature of the chamber.)

5. Data Processing and Measurement Uncertainty

[34] The data are processed after each measurement cycle is completed. Software written in Matlab® is used to automatically load and process the raw data. The software used is similar to that described by *Hanley and Steffes* [2007]. The measured bandwidth (BW_{measured}) of a resonance is a function of the resolution bandwidth (RBW) and the filter response (shape) of the spectrum analyzer which is approximately Gaussian ($1\text{MHz} < \text{RBW} < 2\text{MHz}$) or synchronously tuned 4-pole filter ($300\text{Hz} < \text{RBW} < 300\text{kHz}$). RBW is chosen to be $\sim 1/100$ th of the frequency span. The actual bandwidth is calculated from the measured bandwidth by

$$BW_{\text{actual}} = \sqrt{BW_{\text{measured}}^2 - \text{RBW}^2}. \quad (17)$$

[35] The uncertainties associated with the measurements include instrumental errors (σ_n), errors in dielectric matching (σ_{diel}), transmissivity errors (σ_{trans}), errors due to asymmetry in resonances (σ_{asym}), and errors in measurement conditions (σ_{cond}) due to uncertainties in measurement temperature, pressure and mixing ratio. Electrical noise and instrumental errors arise due to the sensitivity of the electrical devices and their ability to accurately measure the center frequency (f_o) and bandwidth (BW_{measured}). This is calculated as given by *Hanley et al.* [2009] but with additional uncertainties from the external LO used, and is discussed in depth in Appendix A.

[36] Errors due to dielectric matching, transmissivity, and asymmetry are computed in a fashion similar to that used by *Hanley et al.* [2009] for a centimeter-wavelength system, but with modifications to account for the topology of the new measurement system. Errors in dielectric matching are due to the minor misalignments in the center frequency between the loaded and the matched measurements. This is the most trivial error because of the highly accurate software-controlled matching of the center frequency between the loaded and matched measurements. Though the gas used for dielectric matching is lossless, the Q of the resonator can change slightly from that of vacuum values. The magnitude of this effect is calculated by comparing the Q of the three vacuum measurements to that of the dielectric matched measurements.

$$\left(\frac{dQ}{df}\right)_i = \left| \frac{Q_{\text{vac},i} - Q_{\text{matched}}}{f_{\text{vac},i} - f_{\text{matched}}} \right| \quad (18)$$

for $i = 1, 2, \text{ and } 3$

The maximum of the three values is used to calculate a dQ value

$$dQ = \left(\frac{dQ}{df}\right)_{\text{max}} \times |f_{\text{loaded}} - f_{\text{matched}}|, \quad (19)$$

where f_{loaded} and f_{matched} are the center frequencies of the resonances under loaded and matched conditions, respectively. The error in absorptivity due to imperfect dielectric matching is then computed by propagating $\pm dQ$ through equation (9)

$$\sigma_{\text{diel}} = \frac{8.686\pi}{\lambda} \times \left| \left(\frac{1 - \sqrt{t_{\text{loaded}}}}{Q_{\text{loaded}}^m} - \frac{1 - \sqrt{t_{\text{matched}}}}{Q_{\text{matched}}^m + dQ} \right) - \left(\frac{1 - \sqrt{t_{\text{loaded}}}}{Q_{\text{loaded}}^m} - \frac{1 - \sqrt{t_{\text{matched}}}}{Q_{\text{matched}}^m - dQ} \right) \right| \text{ dB/km}. \quad (20)$$

[37] Transmissivity errors are due to the uncertainties in the measurement amplitude. This is caused by the electronics (W band/F band signal generators/detectors), cables, adapters, and waveguides used in the system. Absolute magnitude uncertainties for the signal sources can be safely disregarded since the loaded, matched, and transmissivity measurements are all made with the same signal power. The greatest uncertainty in the transmissivity measurements results from disconnecting and reconnecting the waveguides and cables. Since the waveguides and cables have to be disconnected at least once from the system to characterize their loss, this procedure is repeated two more times to obtain

a better statistical bound on the uncertainty parameters. The standard deviation (s_n) of these measurements is calculated and is weighted by the confidence coefficient for a two-tailed distribution for three samples with a 95% confidence interval [Student, 1908] and is divided by the square root of the number of measurements to yield

$$\sigma_{mt} = \frac{4.303}{\sqrt{3}} s_n. \quad (21)$$

[38] The transmissivity measurements involve sampling the RF power with a WR-10 20 dB directional coupler to feed to the harmonic mixer for down-conversion and detection. This procedure ensures that the RF power input to the harmonic mixer does not exceed its maximum allowed input power of -10 dBm. However, the WR-10 directional coupler does not uniformly sample the input signal throughout the entire frequency range. Hence, an additional 1 dB uncertainty is included in the calculation of the uncertainty due to insertion loss (σ_{ins_loss}). The signal generator has a temperature stability of 1 dB/10°C, but an internal temperature equilibrium is reached after 2 h of operation at a stable ambient temperature [Hewlett-Packard, 1997]. Since the measurement environment outside the temperature chamber is maintained at a constant temperature throughout the measurement cycle, this uncertainty can also be disregarded. The total uncertainty in insertion loss is calculated by

$$\sigma_{ins_loss} = \sigma_{mt} + 1.0 \text{ dB}. \quad (22)$$

[39] The error in insertion loss is used to compute the transmissivity error

$$\sigma_{t,i} = \frac{1}{2} \left(10^{-(S_i - \sigma_{ins_loss})} - 10^{-(S_i + \sigma_{ins_loss})} \right), \quad (23)$$

$i = l, m,$

where l, m are the loaded and matched cases, respectively, and S is the insertion loss of the resonator. This is used to compute the 2σ uncertainties in opacity and is expressed as

$$\sigma_{trans} = \frac{8.686\pi}{2\lambda} \times \left(\frac{\sqrt{t_l + \sigma_{t,l}} - \sqrt{t_l - \sigma_{t,l}}}{Q_{loaded}^m} - \frac{\sqrt{t_m + \sigma_{t,m}} - \sqrt{t_m - \sigma_{t,m}}}{Q_{matched}^m} \right) \text{ dB/km}. \quad (24)$$

[40] Errors from asymmetry are due to the asymmetric nature of the measured resonances which are caused by the overlapping of the off-axis mode resonances on the axial mode resonances. The asymmetric nature of the resonances are more prominent at the shorter wavelengths and colder temperatures. This is likely caused by minor misalignments in mirror positions due to changes in the temperature. Errors due to asymmetry result from the disproportionate asymmetric broadening of the loaded measurements compared to the matched measurements. Equivalent full bandwidths based on assuming symmetry of the high and low sides of the resonances are calculated as

$$BW_{high} = 2 \times (f_{high} - f_{center}), \quad (25)$$

$$BW_{low} = 2 \times (f_{center} - f_{low}), \quad (26)$$

where BW_{high} , BW_{low} , f_{high} , f_{center} , and f_{low} are the high bandwidth, low bandwidth, higher-frequency half power point, center frequency, and lower-frequency half power point, respectively. The difference between the opacities calculated using BW_{high} and BW_{low} (treated as 2σ errors) is defined as σ_{asym} and calculated as

$$\sigma_{asym} = \frac{8.686\pi}{\lambda} \times \left| \left(\frac{1 - \sqrt{t_{loaded}}}{Q_{loaded,high}^m} - \frac{1 - \sqrt{t_{matched}}}{Q_{matched,high}^m} \right) - \left(\frac{1 - \sqrt{t_{loaded}}}{Q_{loaded,low}^m} - \frac{1 - \sqrt{t_{matched}}}{Q_{matched,low}^m} \right) \right| \text{ dB/km}. \quad (27)$$

where $Q_{loaded,high/low}^m$, $Q_{matched,high/low}^m$ are the measured Q s evaluated using the high and low bandwidths for loaded and matched cases, respectively.

[41] The measured uncertainty in temperature, pressure, and mixing ratio contribute to the total uncertainties due to measurement conditions (σ_{cond}). Although σ_{cond} does not directly affect the measurements, it still needs to be accounted for while creating accurate models for opacity based on the experimental data. Since the dependence of σ_{cond} on the opacity and refractivity are not known while making the measurements, this uncertainty is maintained separately from σ_{tot} and is computed as given by Hanley *et al.* [2009]. Thus, the total 95% confidence for the measurement uncertainty is expressed in dB/km as

$$\sigma_{tot} = \sqrt{\sigma_n^2 + \sigma_{diel}^2 + \sigma_{trans}^2 + \sigma_{asym}^2}. \quad (28)$$

[42] To illustrate the percentage contribution of different uncertainties to the total 2σ uncertainty of a typical measurement, the different uncertainties of an ammonia opacity measurement made under simulated jovian conditions are shown in Figures 7 and 8. The dominant factor in the total uncertainty in most cases for the W band system is σ_n and that for the F band system is σ_{trans} . For the cold temperature measurements, σ_{asym} starts to dominate at the shorter wavelengths. The aggregate sensitivities of the system are shown in Figure 9.

6. Applications to the Study of the Jovian Atmospheres

[43] The observable atmospheres of the jovian planets are dominated by hydrogen and helium with small amounts of methane, water, ammonia, hydrogen sulfide, and other gases. The measurement system described in this paper can be used for measurements of the millimeter-wavelength opacity of gases under simulated jovian conditions. Two such possible applications are discussed further.

6.1. Ammonia Measurements

[44] Ammonia (NH_3) is one of the predominant millimeter-wavelength absorbers in the jovian planets due to the presence of a series of inversion lines around 1.25 cm, several strong rotational lines in the submillimeter region, and a strong ν_2 roto-vibrational line at 2.16 mm. The opacity from gaseous ammonia should be accurately known before the potential effects of other absorbing constituents can be assessed. A handful of millimeter-wavelength measurements

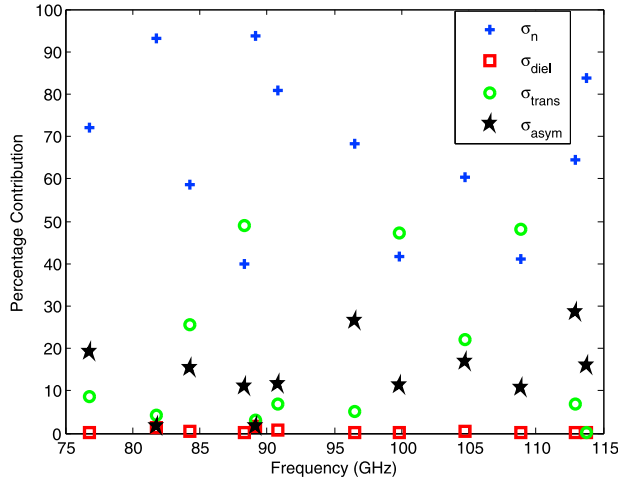


Figure 7. Percentage contribution of the different measurement uncertainties to the total uncertainty of the W band system at room temperature ($T = 297$ K).

of ammonia gas properties under simulated jovian conditions at a single frequency have been made in the past [Joiner and Steffes, 1991; Mohammed and Steffes, 2004]. However, these measurements had very large uncertainties and did not account properly for the adsorption of ammonia on the surface of the resonator. Hence, the opacity models derived based on these measurements do not accurately estimate the millimeter-wavelength opacity of ammonia.

[45] Over 1000 high-accuracy measurements of the absorptive properties of gaseous ammonia under simulated jovian atmospheric conditions have been made using the new measurement system described in this paper [Devaraj et al., 2011]. An example of the ammonia opacity measurements along with the most commonly used opacity formalisms for the H_2/He -broadened NH_3 opacity [Berge and Gulkis, 1976; Spilker, 1990; Joiner and Steffes, 1991; Mohammed and Steffes, 2004; Hanley et al., 2009] is shown

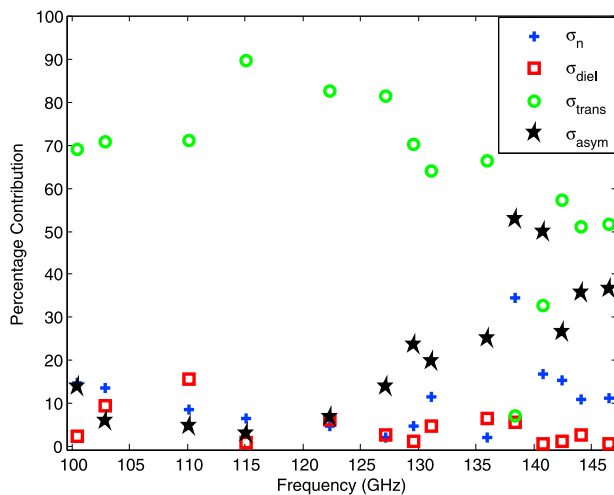


Figure 8. Percentage contribution of the different measurement uncertainties to the total uncertainty of the F band system at $T = 218$ K.

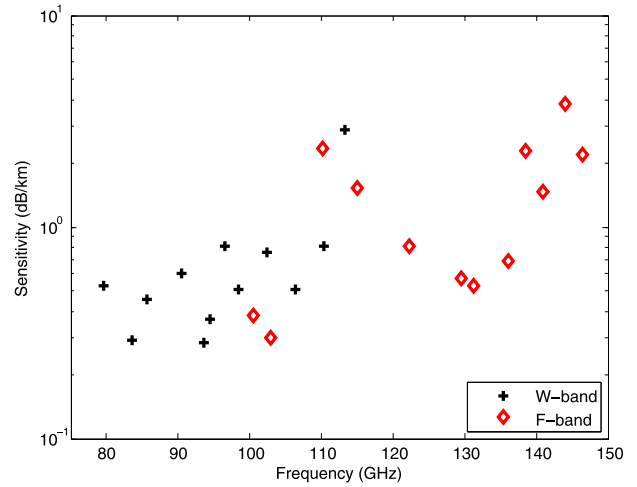


Figure 9. Measured system sensitivity at room temperature ($T = 297$ K) in the 2–4 millimeter-wavelength range.

in Figure 10. These measurements show that none of the existing models accurately predict the opacity of ammonia in the millimeter-wavelength range under simulated jovian atmospheric conditions. Furthermore, none of the models account for the presence of the 2.16 mm ν_2 roto-vibrational line of ammonia [Shimizu, 1969; Chu and Freund, 1973] whose broadening parameters have been measured in the laboratory for the first time under jovian conditions using this new system [Devaraj et al., 2011]. These measurements have been used to create an accurate model for the millimeter-wavelength ammonia opacity from jovian atmospheres [Devaraj et al., 2011].

6.2. Hydrogen Sulfide Measurements

[46] Hydrogen sulfide (H_2S) is a strong millimeter-wavelength absorber in the jovian planets because of the presence of several strong rotational lines in the millimeter-wavelength range (168, 216, and 300 GHz). A single measurement of the H_2/He broadened H_2S opacity was made at 218 GHz at room temperature [Joiner, 1991]. However, this measurement suffered from very large measurement uncertainties because of the crude instrumentation used at that time. Figure 11 shows the predicted normalized opacity (normalized by mixing ratio) of H_2S under simulated jovian conditions using the microwave absorption model developed by DeBoer and Steffes [1994]. The opacity computed using this model might not be accurate for millimeter wavelengths since it was developed based on centimeter-wavelength measurements. High-accuracy millimeter-wavelength measurements of gaseous H_2S at a range of temperatures and pressures that correspond to the altitudes probed by ground-based observations of the jovian planets can be made with the new measurement system to provide insight into the absorptive properties of H_2S .

7. Applications to the Study of the Venus Atmosphere

[47] The atmosphere of Venus is composed mostly of CO_2 ($\sim 96.5\%$), with a small amount of N_2 ($\sim 3.5\%$), and trace amounts of SO_2 , CO , H_2O , H_2SO_4 , and other gases. Gas-

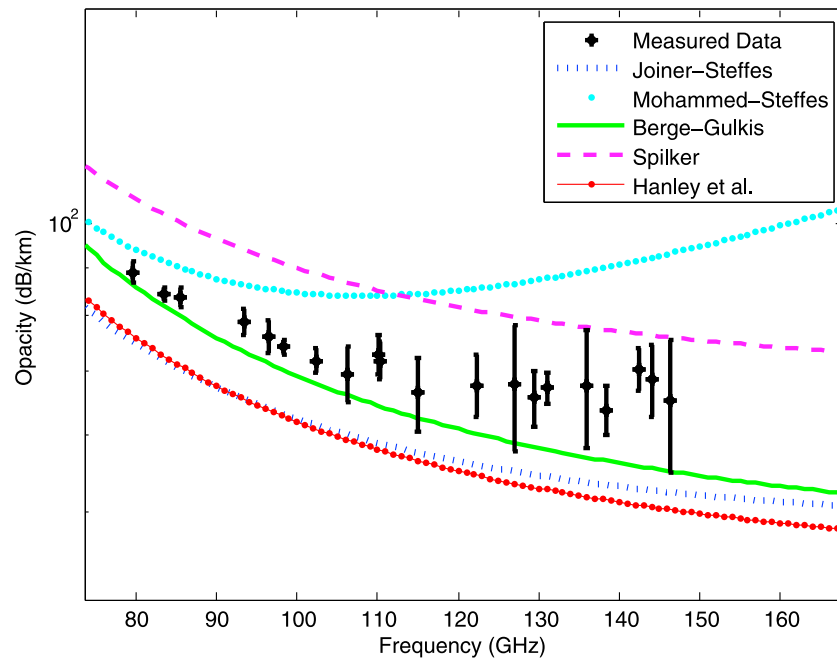


Figure 10. Recent measurements of the opacity of gaseous ammonia using the millimeter-wavelength measurement system along with the error bars. Measurements were taken at a pressure of 1 bar, temperature of 296 K, and a mixing ratio of 3.97% NH_3 , 13.06% He, and 82.97% H_2 . The five commonly used models for the H_2/He -broadened NH_3 opacity [Berge and Gulkis, 1976; Spilker, 1990; Joiner and Steffes, 1991; Mohammed and Steffes, 2004; Hanley et al., 2009] are also shown.

eous SO_2 and H_2SO_4 are highly opaque in the millimeter-wavelength region due to the presence of several rotational transitions in that spectral region. Accurate knowledge of the opacity of such constituents is essential for the interpretation and modeling of the millimeter-wavelength emission spectrum of Venus. The measurement system described in this paper can be used for making high-accuracy measurements of the opacity of gaseous SO_2 and H_2SO_4 under simulated Venus conditions. The atmosphere of Venus is considerably warmer than the jovian atmospheres at the altitude ranges probed by millimeter waves. Hence, an oven capable of operating in the 300–550 K temperature range can be used as the temperature chamber for the measurements of opacity of gaseous SO_2 and H_2SO_4 in a CO_2 atmosphere. A glass transmission cell can be used in place of the resonator inside the oven. Since gaseous SO_2 and H_2SO_4 are highly millimeter-wavelength-opaque, the use of a glass transmission cell with an effective path length of 70 cm would be sufficient for making accurate measurements of their opacity. The signal generators/detectors will be placed outside the oven and energy will be coupled in and out of the transmission cell via horn antennas.

7.1. Sulfur Dioxide Measurements

[48] Previous absorptivity measurements of SO_2 made at 3.2 mm under simulated Venus atmospheric conditions [Fahd, 1992] suffered from large uncertainties because of the crude instrumentation used at that time. Figure 12 shows a plot of the predicted normalized absorptivity (normalized by mixing ratio) of gaseous SO_2 in a CO_2 atmosphere under conditions simulating the cloud base region of Venus. This model is derived using a microwave opacity model

[Suleiman et al., 1996] based on the JPL line catalog [Pickett et al., 1998] and might not be accurate in the millimeter-wavelength range. Accurate millimeter-wavelength opacity measurements of SO_2 under simulated Venus atmospheric conditions are needed to gain insight into the self and foreign gas broadening parameters of SO_2 , and the frequency dependence of absorption. The system described in this paper with minor modifications can be used for making such high-accuracy measurements of the properties

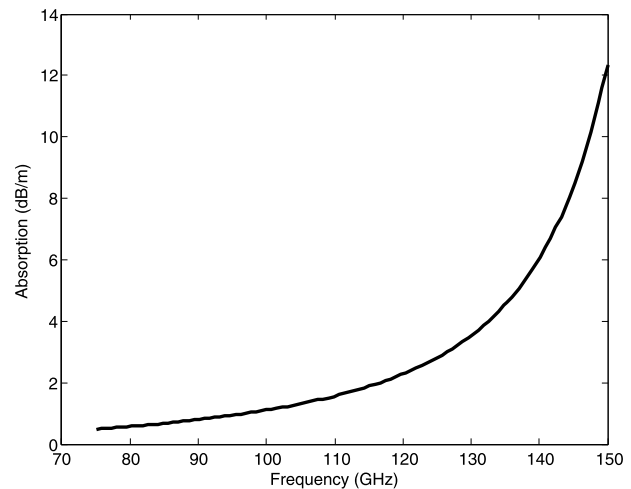


Figure 11. Predicted opacity (normalized by mixing ratio) of gaseous H_2S broadened by H_2/He under simulated jovian atmospheric conditions ($P = 3$ bars, $T = 200$ K, H_2S mixing ratio $\leq 1\%$).

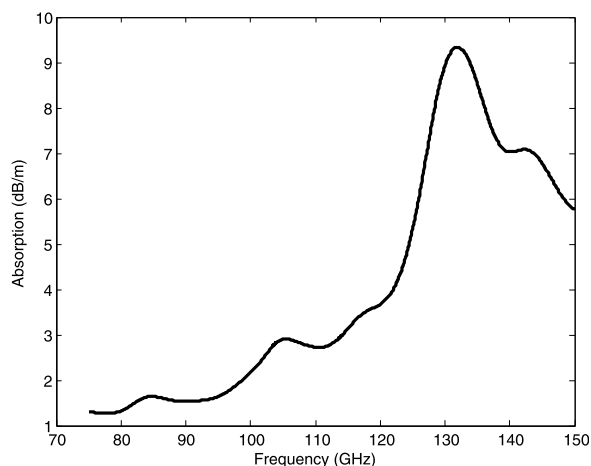


Figure 12. Predicted opacity (normalized by mixing ratio) of gaseous SO_2 broadened by CO_2 under simulated Venus atmospheric conditions ($P = 1$ bar, $T = 375$ K, SO_2 mixing ratio $\leq 1\%$).

of SO_2 in a CO_2 atmosphere at pressures up to 3 bars in the 300–550 K temperature range.

7.2. Sulfuric Acid Vapor Measurements

[49] Previous measurements of the 3.2 mm opacity of H_2SO_4 vapor in a CO_2 atmosphere made by *Fahd* [1992] are of relatively low precision. Figure 13 shows a plot of the predicted normalized absorptivity (normalized by mixing ratio) of H_2SO_4 vapor in a CO_2 atmosphere under conditions simulating the cloud base region of Venus. The Van Vleck-Weisskopf lineshape [Van Vleck and Weisskopf, 1945] and the Gross lineshape [Gross, 1955] are used to predict the absorption from gaseous H_2SO_4 . The models, derived using the JPL line catalog [Pickett et al., 1998], use a self-broadening parameter of 21.6 MHz/torr and a foreign gas broadening parameter of 7.2 MHz/torr. There is a need to estimate the broadening parameters of gaseous H_2SO_4 and verify the accuracy of these models by measuring the absorptivity of H_2SO_4 vapor under Venus atmospheric conditions. The system described in this paper can be used for making such high precision measurements of the millimeter-wavelength opacity of gaseous H_2SO_4 in a CO_2 atmosphere.

[50] Since H_2SO_4 is highly opaque in the millimeter-wavelength range, the FPR can be replaced with a transmission cell thereby providing continuous spectral coverage. The ultrastable sources and detectors should be used external to the temperature chamber and can provide continuum measurements of the opacity. High-gain WR-10 horn antennas attached to the signal source and detector placed outside the oven can be used to transmit signals through and receive signals from the glass transmission cell. The block diagram of such a measurement system is shown in Figure 14. The laboratory measurements of the absorptivity of H_2SO_4 vapor can be used to accurately estimate the self and foreign gas broadening parameters which have thus far been only coarsely estimated.

7.3. Uncertainties in the Observed Millimeter-Wavelength Spectrum of Venus

[51] Millimeter-wavelength observations of Venus made near the 3 mm-wavelength range show a significant day-

night variation in the brightness temperature [de Pater et al., 1991; Sagawa, 2008]. de Pater et al. [1991] made observations of Venus at 2.6 mm with the Hat Creek Interferometer and reported a nightside to dayside variation in the brightness temperature of approximately 30 K. More recent observations of Venus were made with the Nobeyama millimeter-wave array at 103 GHz (~ 3 mm) and a substantial (20%) diurnal variation in the millimeter-wavelength brightness was observed [Sagawa, 2008].

[52] The peak of the weighting function at 3 mm-wavelength occurs at approximately 50 km altitude [Fahd, 1992]. The physical temperature of that region is not likely to be a strong function of local time [Taylor et al., 1980]. Hence, the observed diurnal variation in the brightness temperature in the millimeter-wavelength continuum is most likely due to changes in opacity of the atmosphere at this wavelength. A complete understanding of this measured variation in the emission spectra requires accurate modeling of the effects of the atmospheric constituents of Venus. This requires accurate data concerning the opacities of the constituents. Sagawa [2008] attributes the variations in the brightness temperature to spatial variations in the abundances of gaseous H_2SO_4 and SO_2 in a range of altitudes from just below the lower cloud base to the top of the lower cloud (pressures 0.7–2 bars). Furthermore, SO_2 abundance in and above the cloud region is a possible tracer of active volcanism. The frequency dependence of the millimeter-wavelength absorption from gaseous H_2SO_4 and SO_2 are speculative, since very few of the thousands of the centimeter- and millimeter-wavelength transitions contained in the JPL line catalog [Pickett et al., 1998] have ever been measured. Additionally, Kolodner and Steffes [1998] were unable to fit their measurements of the pressure-broadened centimeter-wavelength (1.3–13.3 cm) opacity from a $\text{CO}_2/\text{H}_2\text{SO}_4$ (gas) mixture characteristic of the Venus atmosphere to a pressure broadened spectrum derived from the catalog.

[53] The abundances of sulfur compounds in the 40–50 km altitude range in Venus have been established by various remote sensing methods, with SO_2 abundance

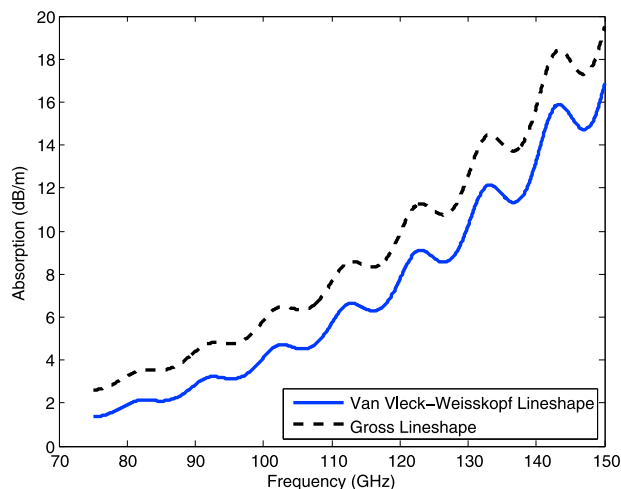


Figure 13. Predicted opacity (normalized by mixing ratio) of H_2SO_4 vapor broadened by CO_2 under simulated Venus atmospheric conditions ($P = 1$ bar, $T = 375$ K, H_2SO_4 mixing ratio $\leq 1\%$).

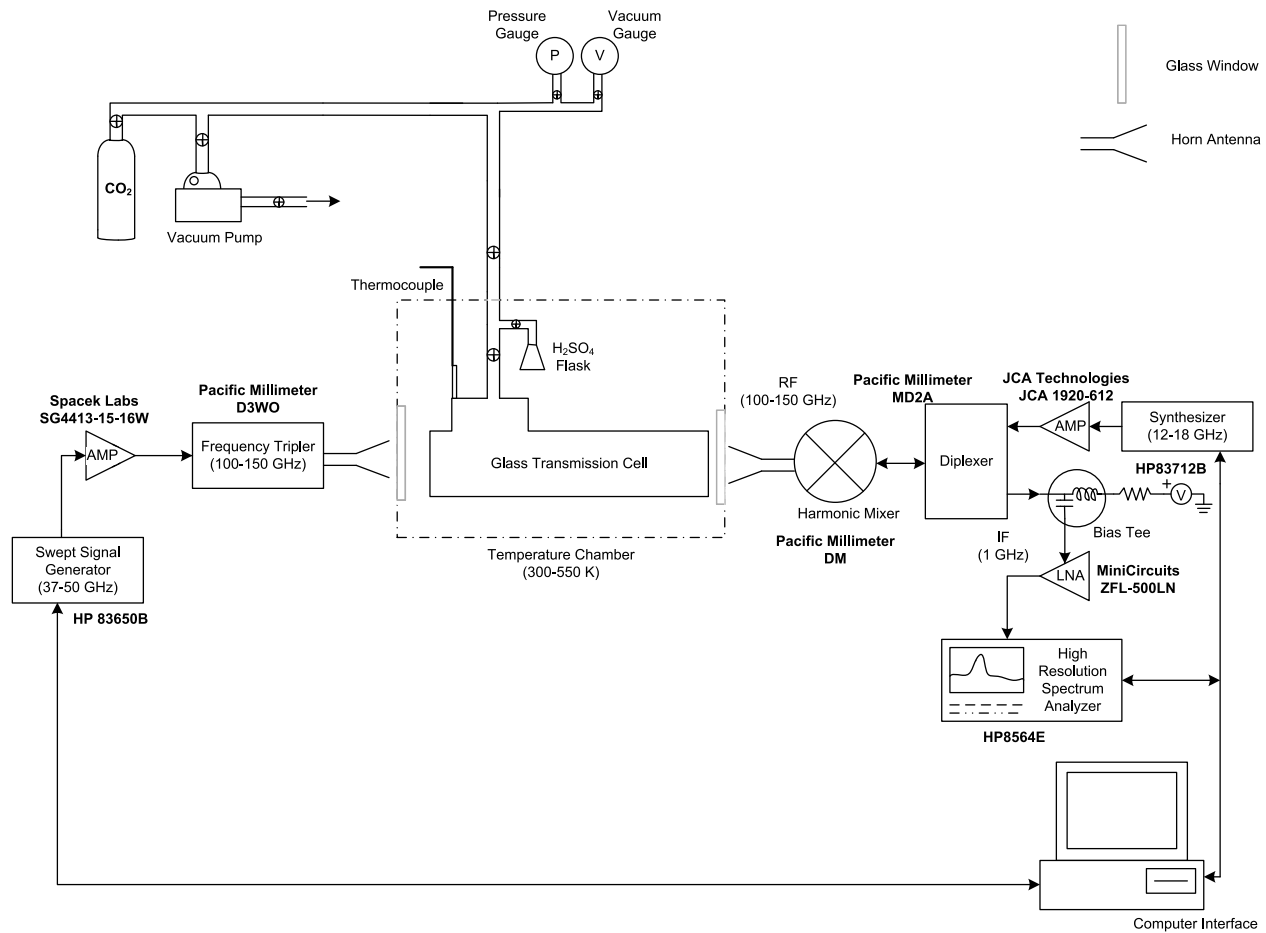


Figure 14. Block diagram of the sulfuric acid vapor F band measurement system.

estimated to be 130 ± 40 ppm [Bézard *et al.*, 1993], and H_2SO_4 abundance between 2–10 ppm depending on the latitude [Kolodner and Steffes, 1998]. Figure 15 shows a plot of the percentage contribution to the total opacity under Venus atmospheric conditions. Collisionally induced dipole moments of CO_2 and N_2 are modeled as per Ho *et al.* [1966]. Collisionally induced absorption from SO_2 is modeled as per Suleiman *et al.* [1996], and H_2SO_4 is modeled using a Gross lineshape and using a self-broadening parameter of 21.6 MHz/torr and a foreign gas broadening parameter of 7.2 MHz/torr. This plot only shows the prediction of contribution to the total 2–4 millimeter-wavelength opacity from the different constituents in the Venus atmosphere and does not represent the actual millimeter-wavelength opacity. It should be noted that predicted contribution to the opacity from H_2SO_4 and more importantly SO_2 is significant. The laboratory measurements of the 2–4 millimeter-wavelength properties of these gases can shed light on the uncertainties in the observed millimeter-wavelength spectrum of Venus.

8. Future Work

[54] Future work will involve extending the wavelength range of the current measurement system and measuring gas properties at shorter wavelengths. The FPR that was built

for the current measurement system has the capability to operate in the 1–4 millimeter-wavelength range. A G band (140–220 GHz) planar frequency doubler and harmonic detectors were recently acquired. The G band doubler

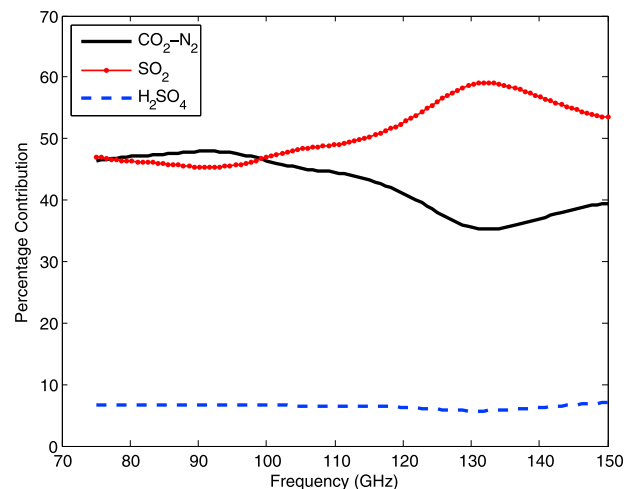


Figure 15. Percentage contribution to the total opacity under Venus conditions ($P = 2.5$ bars; $T = 375$ K; $\text{H}_2\text{SO}_4 = 6$ ppm; $\text{SO}_2 = 150$ ppm; $\text{N}_2 = 0.035$; $\text{CO}_2 = 0.9648$).

along with the AMC can be used to generate the signals in the 1.5–2 millimeter-wavelength range and a series of harmonic mixers can be used for down-conversion. Future work will also involve employing the measurement system for studying the millimeter-wavelength properties of gaseous H_2S under the jovian atmospheric conditions and gaseous SO_2 and H_2SO_4 vapor under Venus atmospheric conditions.

9. Conclusions

[55] Ground-based millimeter-wavelength astronomy is very powerful in probing planets because of the low attenuation millimeter waves suffer in Earth's atmosphere compared to submillimeter waves. New millimeter arrays such as the ALMA are capable of providing an unprecedented combination of sensitivity, angular resolution, spectral resolution, and imaging fidelity. Hence, accurate data concerning the absorptive and refractive properties of various atmospheric constituents are required to interpret the observations and derive planet-wide abundances of these constituents. Measurements of ammonia opacity made with the measurement system described in this paper have unequivocally proven that the existing models do not accurately predict the opacity of ammonia in the millimeter-wavelength range under simulated planetary conditions [Devaraj *et al.*, 2011]. Hence, there is a need to accurately measure the millimeter-wavelength properties of gases such as H_2S , SO_2 , and H_2SO_4 under simulated planetary conditions. The system described in this paper can be used for making such high-precision measurements. Furthermore, the measurement system can also be used for numerous other spectroscopic studies under terrestrial conditions.

Appendix A: Instrumental Errors

[56] Electrical noise arises from the noise of the internal electronics and the accuracies of the frequency references. Electrical noise is uncorrelated and the best estimate of instrumental uncertainty is the mean of multiple measurements. The variance of the best error estimate is given by the sample variance (S_N^2) weighted by the confidence coefficient (B) as

$$\sigma_N^2 = B \times \frac{S_N^2}{N}, \quad (\text{A1})$$

where N is the number of independent measurements of the sample. Five sets of independent measurements are taken and a confidence coefficient corresponding to the 95% confidence interval is used. The confidence coefficient is equal to the critical value of the Student's t test [Student, 1908] for a two-tailed significance of 0.05 and $N-1$ degrees of freedom. This means that the true mean will fall above the confidence interval 2.5% of the time and below the confidence interval 2.5% of the time. The confidence coefficient used for our measurements is 2.776.

[57] The spectrum analyzer is used for measuring the resonances and the manufacturer specified uncertainties are the 3σ values [Hewlett-Packard, 1997]. The 3σ standard

deviation for the center frequency and bandwidth measurements, respectively, are estimated by

$$\sigma_o \leq \pm (f_o \times f_{ref\ acc} + 0.05 \times SPAN + 0.15 \times RBW + 10) \text{ (Hz)}, \quad (\text{A2})$$

$$\sigma_{BW} \leq \pm (BW_{measured} \times f_{ref\ acc}) + 4 \times N_H + 2 \times LSD \text{ (Hz)}, \quad (\text{A3})$$

where $f_{ref\ acc}$ is given as

$$f_{ref\ acc} = (\text{aging} \times \text{time since calibration}) + \text{initial achievable accuracy} + \text{temperature stability}, \quad (\text{A4})$$

and f_o , $SPAN$, RBW , BW_{actual} , N_H , and LSD are the center frequency, frequency span, resolution bandwidth, actual frequency bandwidth, harmonic number, and least significant digit of the bandwidth measurement, respectively. LSD is calculated as $LSD = 10^x$ for the smallest positive integer value of x such that $SPAN < 10^{x+4}$. These formulae are for $SPAN > 2 \text{ MHz} \times N_H$, which is a wide-span scenario. For $SPAN \leq 2 \text{ MHz} \times N_H$, $SPAN$ multiplication factor of 0.05 is replaced with 0.01. For the spectrum analyzer used in the experiments, $f_{ref\ acc}$ reduces to

$$f_{ref\ acc} = (10^{-7} \times \text{years since calibrated}) + 3.2 \times 10^{-8}. \quad (\text{A5})$$

[58] The formulae for calculating σ_o and σ_{BW} represent the 3σ uncertainties and are scaled by 2/3 to obtain the 2σ uncertainties. There is a 3σ uncertainty associated with the RBW ($\pm 25\%$). However, this changes the value of BW_{actual} (equation (17)) by less than 0.01% and hence can be omitted for all practical purposes in the computation of the measurement uncertainties. The worst case scenario (greatest error) is considered in the computation of uncertainties of the instrumental error and electrical noise and is computed as given by DeBoer and Steffes [1994]

$$\sigma_\psi^2 = \langle \Gamma_l^2 \rangle + \langle \Gamma_m^2 \rangle - 2\langle \Gamma_l \Gamma_m \rangle, \quad (\text{A6})$$

where

$$\langle \Gamma_i^2 \rangle = \frac{\gamma_i^2}{f_{oi}^2} \left[\frac{\sigma_o^2}{Q_i^2} + \sigma_{BW}^2 + \sigma_{Ni}^2 + \frac{2\sigma_o\sigma_{BW}}{Q_i} \right], \quad (\text{A7})$$

$$i = l, m,$$

$$\langle \Gamma_l \Gamma_m \rangle = -\frac{\gamma_l \gamma_m}{f_{ol} f_{om}} \times \left[\frac{\sigma_o^2}{Q_l Q_m} + \sigma_{BW}^2 + \frac{\sigma_o \sigma_{BW}}{Q_l} + \frac{\sigma_o \sigma_{BW}}{Q_u} \right], \quad (\text{A8})$$

$$Q_i = \frac{f_{oi}}{f_{BW_i}}, \quad i = l, m, \quad (\text{A9})$$

$$\gamma_i = 1 - \sqrt{t}, \quad i = l, m, \quad (\text{A10})$$

where l, m denote loaded and dielectrically matched cases, respectively, and $f_{ol,om}$, and f_{BW_l, BW_m} represent center

frequency, and bandwidth of loaded and dielectrically matched cases, respectively. The 2σ uncertainty of the measured gas absorption due to instrumental errors is given by

$$\sigma_n = \frac{8.686\pi}{\lambda} \sigma_\psi \text{ dB/km}, \quad (\text{A11})$$

where λ is the wavelength in km.

[59] **Acknowledgments.** This work is supported by the NASA Planetary Atmospheres Program under grant NNG06GF34G. The authors wish to thank Thomas R. Hanley for his valuable suggestions and contributions to the Fabry-Perot resonator design and the data processing software.

References

- Berge, G. L., and S. Gulkis (1976), Earth-based radio observations of Jupiter: Millimeter to meter wavelengths, in *Jupiter: Studies of the Interior, Atmosphere, Magnetosphere, and Satellites*, edited by T. Gehrels, pp. 621–692, Univ. of Ariz. Press, Tuscon.
- Bézar, B., C. de Bergh, B. Fegley, J. Maillard, D. Crisp, T. Owen, J. B. Pollack, and D. Grinspoon (1993), The abundance of sulfur dioxide below the clouds of Venus, *Geophys. Res. Lett.*, **20**, 1587–1590.
- Bleaney, B., and R. P. Penrose (1947), The inversion spectrum of ammonia at centimetre wave-lengths, *Proc. R. Soc. A*, **189**, 358.
- Chu, F. Y., and S. M. Freund (1973), Millimeterwave rotation-inversion transition of $^{14}\text{NH}_3$ and $^{15}\text{NH}_3$ in the ν_2 -state, *J. Mol. Spectrosc.*, **48**, 183–184.
- Culshaw, W. (1960), High resolution millimeter wave Fabry-Perot interferometer, *IRE Trans. Microwave Theory Tech.*, **8**, 182–189.
- Culshaw, W. (1961), Resonators for millimeter and submillimeter wave-lengths, *IRE Trans. Microwave Theory Tech.*, **9**, 135–144.
- Culshaw, W. (1962), Further considerations on Fabry-Perot type resonators, *IRE Trans. Microwave Theory Tech.*, **10**, 331–339.
- DeBoer, D. R., and P. G. Steffes (1994), Laboratory measurements of the microwave properties of H_2S under simulated Jovian conditions with an application to Neptune, *Icarus*, **109**, 352–366.
- de Pater, I., F. P. Schloerb, and A. Rudolph (1991), Venus imaged with the Hat Creek interferometer in the $J = 1-0$ CO line, *Icarus*, **90**, 282–298.
- Devaraj, K., P. G. Steffes, and B. M. Karpowicz (2011), Reconciling the centimeter- and millimeter-wavelength ammonia absorption spectra under jovian conditions: Extensive millimeter-wavelength measurements and a consistent model, *Icarus*, **212**, 224–235.
- Dunn, D. E., I. de Pater, M. R. Wright, M. R. Hogerheijde, and L. A. Molnar (2005), High-quality BiMA-OVRO images of Saturn and its rings at 1.3 and 3 millimeters, *Astron. J.*, **129**, 1109–1116.
- Fahd, A. K. (1992), Study and interpretation of the millimeter-wave spectrum of Venus, Ph.D. dissertation, Ga. Inst. of Technol., Atlanta.
- Fahd, A. K., and P. G. Steffes (1992), Laboratory measurements of the microwave and millimeter-wave opacity of gaseous sulfur-dioxide (SO_2) under simulated conditions for the Venus atmosphere, *Icarus*, **97**, 200–210.
- Gordy, W. (1948), Microwave spectroscopy, *Rev. Mod. Phys.*, **20**.
- Griffin, M. J., and G. S. Orton (1993), The near-millimeter brightness temperature spectra of Uranus and Neptune, *Icarus*, **105**, 537–547.
- Griffin, M. J., P. A. R. Ade, G. S. Orton, E. I. Robson, W. K. Gear, I. G. Nolt, and J. V. Radostitz (1986), Submillimeter and millimeter observations of Jupiter, *Icarus*, **65**, 244–256.
- Gross, E. P. (1955), Shape of collision-broadened spectral lines, *Phys. Rev.*, **97**, 395–403.
- Hanley, T. R., and P. G. Steffes (2007), A high-sensitivity laboratory system for measuring the microwave properties of gases under simulated conditions for planetary atmospheres, *Radio Sci.*, **42**, RS6010, doi:10.1029/2007RS003693.
- Hanley, T. R., P. G. Steffes, and B. M. Karpowicz (2009), A new model of the hydrogen and helium-broadened microwave opacity of ammonia based on extensive laboratory measurements, *Icarus*, **202**, 316–335.
- Herriott, D. R., H. Kogelnik, and R. Kompfner (1964), Off axis paths in spherical mirror interferometers, *Appl. Opt.*, **3**, 523–526.
- Hewlett-Packard (1997), HP 8560 E-Series Spectrum Analyzer Calibration Guide, Santa Rosa, Calif.
- Ho, W., I. A. Kaufman, and P. Thaddeus (1966), Laboratory measurements of microwave absorption models of the atmosphere of Venus, *J. Geophys. Res.*, **71**, 5091–5108.
- Joiner, J. (1991), Millimeter-wave spectra of the Jovian planets, Ph.D. dissertation, Ga. Inst. of Technol., Atlanta.
- Joiner, J., and P. G. Steffes (1991), Modeling of Jupiter's millimeter wave emission utilizing laboratory measurements of ammonia (NH_3) opacity, *J. Geophys. Res.*, **96**, 17,463–17,470.
- Kolodner, M. A., and P. G. Steffes (1998), The microwave absorption and abundance of sulfuric acid vapor in the Venus atmosphere based on new laboratory measurements, *Icarus*, **132**, 151–169.
- Kramer, C., R. Moreno, and A. Greve (2008), Long-term observations of Uranus and Neptune at 90 GHz with IRAM 30m telescope, *Astron. Astrophys.*, **482**, 359–363.
- Lamarre, J. M., et al. (2003), The Planck high frequency instrument, a third generation CMB experiment, and a full sky submillimeter survey, *New Astron. Rev.*, **47**, 1017–1024.
- Lellouch, E. (2008), Planetary atmospheres with ALMA, *Astrophys. Space Sci.*, **313**, 175–181.
- Matthaei, G. L., L. Young, and E. Jones (1980), *Microwave Filters, Impedance Matching Networks and Coupling Structures*, McGraw-Hill, New York.
- Mohammed, P. N., and P. G. Steffes (2004), Laboratory measurements of the W band (3.2 mm) properties of phosphine (PH_3) and ammonia (NH_3) under simulated conditions for the outer planets, *J. Geophys. Res.*, **109**, E07S13, doi:10.1029/2003JE002201.
- Muhleman, D. O., and G. L. Berge (1991), Observations of Mars, Uranus, Neptune, Io, Europa, Ganymede and Callisto at a wavelength of 2.66 mm, *Icarus*, **92**, 263–272.
- Pickett, H. M., R. L. Poynter, E. A. Cohen, M. L. Delitsky, J. C. Pearson, and H. S. P. Müller (1998), Submillimeter, millimeter, and microwave spectral line catalog, *J. Quant. Spectrosc. Radiat. Transfer*, **60**, 883–890.
- Rodrigues, C. C., and D. Moraes Jr. (2002), Control of the emission of ammonia through adsorption in a fixed bed of activated carbon, *Adsorpt. Sci. Technol.*, **20**, 1013–1022.
- Sagawa, H. (2008), Terahertz remote sensing of the Venusian atmosphere: Observations using the Nobeyama millimeter array, *J. Natl. Inst. Inf. Commun. Technol. (Jpn.)*, **55**, 149–157.
- Shimizu, F. (1969), Dipole moment of NH_3 in the ν_2 excited state, *J. Chem. Phys.*, **51**, 2754–2755.
- Spilker, T. R. (1990), Laboratory measurements of the microwave absorptivity and refractivity spectra of gas mixtures applicable to giant planet atmospheres, Ph.D. dissertation, Stanford Univ., Stanford, Calif.
- Student (1908), The probable error of a mean, *Biometrika*, **6**, 1–25.
- Suleiman, S. H., M. A. Kolodner, and P. G. Steffes (1996), Laboratory measurement of the temperature dependence of gaseous sulfur dioxide (SO_2) microwave absorption with application to the Venus atmosphere, *J. Geophys. Res.*, **101**, 4623–4635.
- Taylor, F. W., et al. (1980), Structure and meteorology of the middle atmosphere of Venus: Infrared remote sensing from the Pioneer orbiter, *J. Geophys. Res.*, **85**, 7962–8006.
- Valkenburg, E. P., and V. E. Derr (1966), A high-Q Fabry-Perot interferometer for water vapor absorption measurements in the 100 Gc/s to 300 Gc/s frequency range, *Proc. IEEE*, **54**, 493–498.
- van der Tak, F., I. de Pater, A. Silva, and R. Millan (1999), Time variability in the radio brightness distribution of Saturn, *Icarus*, **142**, 125–147.
- Van Vleck, J. H., and V. F. Weisskopf (1945), On the shape of collision-broadened lines, *Rev. Mod. Phys.*, **17**, 227–236.
- Weidner, R. T. (1947), Microwave spectrum of iodine monochloride at 4.5 centimeters wavelengths, *Phys. Rev.*, **72**, 1268.
- Young, D. M., and A. D. Crowell (1962), *Physical Adsorption of Gases*, Butterworths, London.
- Zimmerer, R. W. (1963), Spherical mirror Fabry-Perot resonators, *IRE Trans. Microwave Theory Tech.*, **11**, 371–379.

K. Devaraj and P. G. Steffes, School of Electrical and Computer Engineering, Georgia Institute of Technology, 777 Atlantic Dr., Atlanta, GA 30332-0250, USA. (kdevaraj@ece.gatech.edu; steffes@gatech.edu)